MOX-Report No. 44/2019

An XFEM/DG approach for fluid-structure interaction problems with contact

Formaggia, L.; Gatti, F.; Zonca, S.

MOX, Dipartimento di Matematica
Politecnico di Milano, Via Bonardi 9 - 20133 Milano (Italy)

mox-dmat@polimi.it http://mox.polimi.it

An XFEM/DG approach for fluid-structure interaction problems with contact

Luca Formaggia[♯] and Federico Gatti[♯] and Stefano Zonca[♯]

November 19, 2019

[♯] MOX – Modelling and Scientific Computing
Dipartimento di Matematica, Politecnico di Milano
Piazza Leonardo da Vinci, 20133 Milano, Italy
luca.formaggia@polimi.it
federico4.gatti@mail.polimi.it
stefano.zonca@polimi.it

Keywords: fluid-structure interaction contact extended finite element method discontinuous Galerkin Nitsche's method.

Abstract

In this work, we address the problem of fluid-structure interaction with moving structures that may come into contact. We propose a penalization contact algorithm implemented in an unfitted numerical framework designed to treat large displacements. In the proposed method, the fluid mesh is fixed and the structure meshes are superimposed to it without any constraint on the conformity. Thanks to the Extended Finite Element Method (XFEM), we can treat discontinuities of the fluid solution on the mesh elements intersecting the structure; the coupling conditions at the fluid-structure interface are enforced via a discontinuous Galerkin mortaring technique, which is a penalization method that ensures the consistency of the scheme with the underlining problem. Concerning the contact problem, we consider a frictionless contact model in a master/slave approach. Finally, we perform some numerical tests in the case of contact between a flexible body and a rigid wall and between two deformable structures.

1 Introduction

Many engineering applications involve the interaction between a fluid and moving structures, see e.g. [30, 59, 52, 9, 10, 58]. The numerical simulation of such phenomena is very challenging since the structures are subject to large displacements and deformations and special numerical methods are required to handle the movement of

the computational grids. Some applications involve the interaction between structures that may come into contact, see e.g. [49, 43, 42, 47]. A well-established approach to deal with the fluid-structure interaction (FSI) problem is the Arbitrary Lagrangian Eulerian approach (ALE), see e.g. [29, 39, 31]. Its basic idea is to introduce a new reference framework for the fluid domain that follows the movement of the boundary induced by the displacement of the structures. At the discrete level, this permits the fluid mesh to deform in accordance with the structures maintaining its conformity with the interface. However, when the displacements are too large, this approach may fail since inverted fluid elements may appear, or may lead to an inaccurate solution due to the presence of very stretched fluid elements. The same argument can be applied when two structures approach each other. A possible remedy is to remesh, or to locally adapt, the fluid mesh, see e.g. [55, 8]. An alternative is to use the so-called unfitted methods. Unfitted methods rely on a fixed background grid for the fluid, while the structural elements are overlapped to it without any constraint and they are able to move independently from the fluid mesh. This class of methods includes, for example, the Immersed Boundary method [49, 50, 45, 13, 14, 16, 37, 15], the Fictitious Domain method [36, 48, 7, 12], the Fully-Eulerian approach [54, 51, 53, 34], the Extended Finite Element method (XFEM) [35, 23, 4, 61, 56], the Cut-Finite Element method [44], the Polygonal Discontinuous Galerkin method [5].

Regarding the contact problem, several models have been proposed in the context of pure contact mechanics, see e.g. [40, 57]. The classical model describes the contact via the Karush-Kuhn-Tucker conditions

$$\Delta \geq 0, \qquad \lambda \leq 0, \qquad \lambda\Delta = 0,$$

where Δ is the distance between structures and λ is the normal traction at the structure interface. It requires to introduce variational inequalities and the resulting constraints can be imposed, for instance, via a penalization approach, see e.g. [26]. Recent works use an augmented Lagrangian / Nitsche's approach to include the contact in the discrete formulation, which is a penalization approach with the advantage that it leads to a consistent formulation, see e.g. [25, 24, 27, 28, 19, 20]. However only few results have been proposed regarding the contact in the fluid-structure interaction framework, see e.g. [33, 18, 1, 2]. In the present work we employ the XFEM [46, 11, 38] in combination with the discontinuous Galerkin (DG) mortaring [6, 22] to discretize a FSI problem with contact. The XFEM is based on the classical Finite Element method (FEM) with the advantage of enriching the numerical approximation on the fluid elements crossed by the structure. In particular, it allows to treat discontinuities within an element and, for example, to represent jumps in the numerical solution. The DG approach allows to couple the fluid and structure problems at the unfitted interface. To handle the contact between the immersed structures, we employ a penalization method that prescribes the non-penetration condition at the solid-solid interface.

The aim of this work is to illustrate the XFEM/DG procedure and present some preliminary results. In Section 2, we introduce the fluid-structure interaction model and its XFEM/DG formulation; in Section 3, we present the contact model and the discrete approximation in the XFEM/DG context; in Section 4, we show some numerical

test cases; finally in Section 5, we draw the conclusions and discuss possible future developments.

2 Unfitted approach for fluid-structure interaction

In this section, we introduce the governing equations for the fluid-structure interaction problem and its discretization in the XFEM/DG formulation.

2.1 Fluid-structure interaction model

We consider the fluid and solid domains $\Omega^f(t)$ and $\Omega^s(t)$ and we partition their boundaries $\partial\Omega^f(t)$ and $\partial\Omega^s(t)$, equipped with the outward unit normal $\mathbf{n}^f(t)$ and $\mathbf{n}^s(t)$, as $\partial\Omega^f(t) = \Sigma(t) \cup \Gamma^f$ and $\partial\Omega^s(t) = \Sigma(t) \cup \Gamma^s$, where $\Sigma(t) = \overline{\Omega}^f(t) \cap \overline{\Omega}^s(t)$ is the fluid-structure interface with the time dependent unit normal $\mathbf{n}(t) = \mathbf{n}^s(t) = -\mathbf{n}^f(t)$, and Γ^f and Γ^s are the portions of the boundaries fixed in time, see Figure 1. Moreover, we indicate with $\Omega = \Omega^f(t) \cup \Omega^s(t)$.

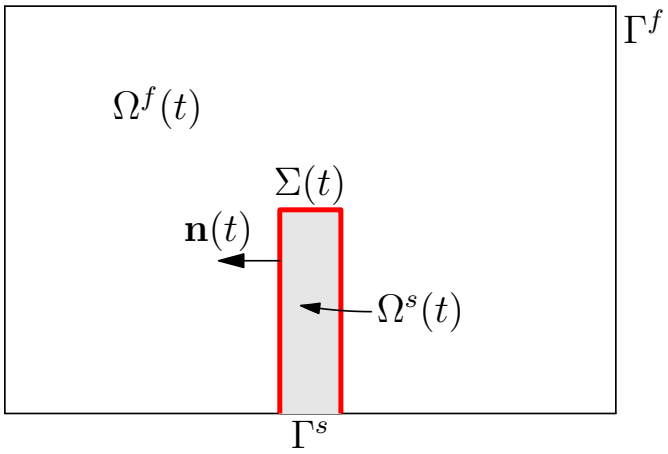

Figure 1: Sketch of the fluid and structure domains $\Omega^f(t)$ (white) and $\Omega^s(t)$ (grey) with the fluid-structure interface $\Sigma(t)$ (red).

The FSI problem in d-dimensions (with $d = 2, 3$) reads as follows:
Find, for any $t \in (0, T]$, the fluid velocity $\mathbf{u}(t) : \Omega^f(t) \to \mathbb{R}^d$, the fluid pressure $p(t) : \Omega^f(t) \to \mathbb{R}$, the solid displacement $\widehat{\mathbf{d}}(t) : \widehat{\Omega}^s \to \mathbb{R}^d$, such that:

$$\begin{cases} \rho^f \partial_t \mathbf{u} + \rho^f \mathbf{u} \cdot \nabla \mathbf{u} - \nabla \cdot \mathbf{T}^f(\mathbf{u}, p) = \mathbf{f}^f, & \text{in } \Omega^f(t), \\ \nabla \cdot \mathbf{u} = 0, & \text{in } \Omega^f(t), \\ \mathbf{u} = \mathbf{0}, & \text{on } \Gamma^f; \end{cases} \tag{1}$$

$$\begin{cases} \rho^s \partial_{tt} \widehat{\mathbf{d}} - \nabla \cdot \widehat{\mathbf{T}}^s(\widehat{\mathbf{d}}) = \widehat{\mathbf{f}}^s, & \text{in } \widehat{\Omega}^s, \\ \widehat{\mathbf{d}} = \mathbf{0}, & \text{on } \widehat{\Gamma}^s; \end{cases} \tag{2}$$

$$\begin{cases} \mathbf{u} = \dot{\mathbf{d}}, & \text{on } \Sigma(t), \\ \mathbf{T}^f(\mathbf{u}, p)\mathbf{n} = \mathbf{T}^s(\mathbf{d})\mathbf{n}, & \text{on } \Sigma(t). \end{cases} \tag{3}$$

Notice that, we consider the fluid problem (1) and the coupling conditions (3) in the Eulerian configuration, while the structure problem (2) is written in the Lagrangian framework. We use the $\widehat{\cdot}$ notation to indicate the Lagrangian quantities, recalling that we can pass from the reference to the current configuration with the Lagrangian map $\widehat{\mathcal{L}}(t) : \widehat{\Omega}^s \to \Omega^s(t)$ and that we can relate a function f in the current configuration with its reference counterpart as follows:

$$f(\mathbf{x}, t) = f \circ \widehat{\mathcal{L}}(t) = \widehat{f}(\widehat{\mathbf{x}}, t).$$

For the fluid problem (1), we consider the Navier-Stokes equations for an incompressible fluid with density ρ^f and Cauchy stress tensor $\mathbf{T}^f(\mathbf{u}, p) = -p\mathbf{I} + 2\mu^f\mathbf{D}(\mathbf{u})$, where μ^f is the dynamic viscosity and $\mathbf{D}(\mathbf{v}) = \frac{\nabla\mathbf{v}+\nabla\mathbf{v}^T}{2}$. For the solid problem (2), we consider the equations of elastodynamics, indicating with ρ^s the density of the material and by $\widehat{\mathbf{T}}^s(\widehat{\mathbf{d}})$ the Piola-Kirchhoff stress tensor, linked to the Cauchy stress tensor $\mathbf{T}^s(\mathbf{d})$ by the following formula:

$$\widehat{\mathbf{T}}^s = J\mathbf{T}^s\mathbf{F}^{-T}.$$

Here, $J = \det(\mathbf{F})$ and $\mathbf{F} = \nabla\widehat{\mathcal{L}} = \mathbf{I} + \nabla\widehat{\mathbf{d}}$ is the deformation gradient. We indicate the external forces acting on the fluid and on the solid by $\mathbf{f}^f$ and $\widehat{\mathbf{f}}^s$, respectively, and we apply homogeneous Dirichlet boundary conditions on Γ^f and $\widehat{\Gamma}^s$.

Finally, to close the system (1)-(3), we define the initial conditions for fluid velocity, solid displacement and solid velocity:

$$\begin{aligned} &\mathbf{u}(\mathbf{x}, 0) = \mathbf{u}^0(\mathbf{x}), && \text{in } \Omega^f(0), \\ &\partial_t\widehat{\mathbf{d}}(\mathbf{x}, 0) = \widehat{\mathbf{v}}^0(\mathbf{x}), \quad \widehat{\mathbf{d}}(\mathbf{x}, 0) = \widehat{\mathbf{d}}^0(\mathbf{x}), && \text{in } \widehat{\Omega}^s. \end{aligned}$$

2.2 Numerical discretization

We introduce the background mesh $\mathcal{T}_h$ that discretizes the entire domain Ω and the solid mesh $\mathcal{T}_h^s(t)$ that covers the domain $\Omega^s(t)$. The background mesh $\mathcal{T}_h$ is fitted to $\partial\Omega$ but in general not to $\Sigma(t)$. The mesh $\mathcal{T}_h^s(t)$ overlaps $\mathcal{T}_h$, as shown in Figure 2. Notice that there are some elements $K \in \mathcal{T}_h$ that are partially overlapped by $\mathcal{T}_h^s(t)$, and thus split by $\Sigma(t)$ into two or more polyhedra P_K, see Figure 3. We denote these elements as *cut-elements* and we collect them in the set $\mathcal{G}_h(t)$ defined as:

$$\mathcal{G}_h(t) = \{K \in \mathcal{T}_h : K \cap \Sigma(t) \neq \emptyset\}.$$

The Extended Finite Element method allows to duplicate the set of degrees of freedom (dofs) associated with any element $K \in \mathcal{G}_h(t)$ and, for each set, to compute a numerical solution on a polyhedron P_K of the element K that belongs to the fluid domain. It is important to point out that although the background mesh $\mathcal{T}_h$ is fixed, the intersection

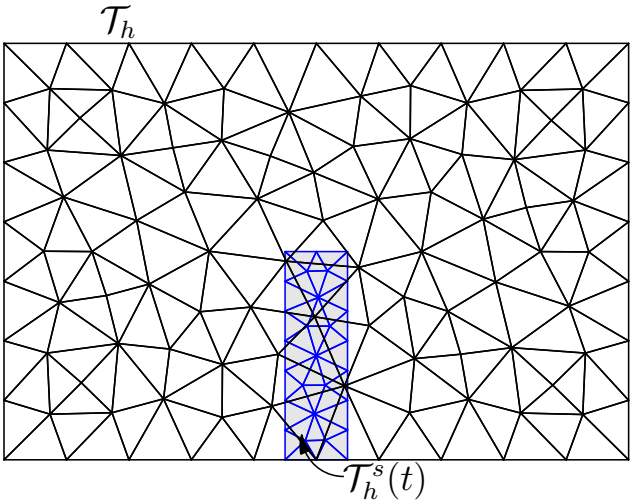

Figure 2: The structure mesh $\mathcal{T}_h^s(t)$ (grey elements with blue edges) overlaps the background mesh $\mathcal{T}_h$.

with the foreground mesh $\mathcal{T}_h^s(t)$ changes in time due to the movement of the solid body, so that the background fluid elements crossed by $\Sigma(t)$ may change from a time step to the following one. We denote by $\mathcal{F}_{\mathcal{G},h}(t)$ the set of faces F of the elements in $\mathcal{G}_h(t)$, see Figure 3. The elements $K \in \mathcal{T}_h$ completely overlapped by $\mathcal{T}_h^s(t)$ do not contribute in the numerical formulation since they do not represent a physical portion of the domain. Further details can be found in [32, 61].

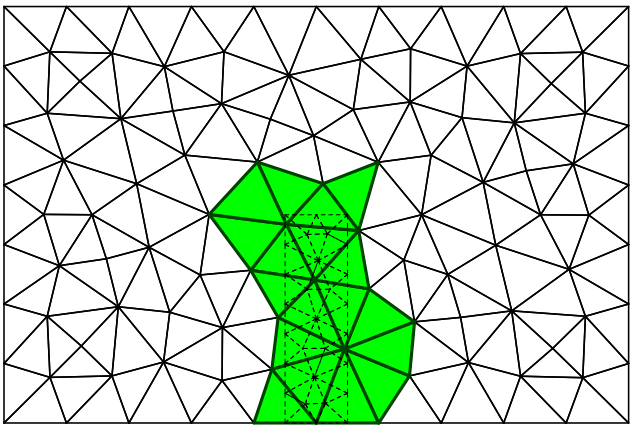

Figure 3: Representation (in green) of the set of background elements partially overlapped $\mathcal{G}_h(t)$ and the corresponding set of faces $\mathcal{F}_{\mathcal{G},h}(t)$.

The presence of cut-elements may compromise the stability of the numerical formulation. Indeed, the intersection between the background and the solid meshes may generate small polyhedral elements and hamper the conditioning of the resulting dis-

crete formulation. A possible remedy is to introduce a stabilization term, the so-called *ghost penalty* term, see e.g. [21], which prevents the ill-conditioning of the discrete problem.

The space discretization is based on linear finite elements for the fluid velocity, pressure and solid displacement, defined as follows:

$$\mathbf{V}_h(t) = \{\mathbf{v}_h \in [X_h^f(t)]^d : \mathbf{v}_{h|\Gamma^f} = 0\}, \quad Q_h(t) = \{q_h \in X_h^f(t)\},$$
$$\widehat{\mathbf{W}}_h = \{\widehat{\mathbf{w}}_h \in [\widehat{X}_h^s]^d : \widehat{\mathbf{w}}_{h|\widehat{\Gamma}^s} = 0\},$$

where the finite element space for the fluid $X_h^f(t)$ is the direct sum of two spaces, one for the standard FEM part, i.e. for all the elements $K \notin \mathcal{G}_h(t)$, and one for the "extended" part, i.e. for all $K \in \mathcal{G}_h(t)$, namely

$$X_h^f(t) = X_h^{f,std}(t) \bigoplus X_h^{f,XFEM}(t),$$
$$X_h^{f,std}(t) = \{v_h \in \mathcal{C}^0(\Omega^f(t)) : v_{h|K} \in \mathbb{P}_1(K), \forall K \in \mathcal{T}_h \setminus \mathcal{G}_h(t)\},$$
$$X_h^{f,XFEM}(t) = \{v_h \in \mathcal{C}^0(\Omega^f(t)) : v_{h|P_K} \in \mathbb{P}_1(P_K), \forall P_K \in K, \forall K \in \mathcal{G}_h(t)\},$$

while

$$\widehat{X}_h^s = \{\widehat{w}_h \in \mathcal{C}^0(\widehat{\Omega}^s) : \widehat{w}_{h|K} \in \mathbb{P}_1(K), \forall K \in \widehat{\mathcal{T}}_h^s\}.$$

The proposed semi-discrete formulation of the problem described by equation (1)-(3) reads as follows:
For any $t > 0$, find $(\mathbf{u}_h(t), p_h(t), \widehat{\mathbf{d}}_h(t)) \in \mathbf{V}_h(t) \times Q_h(t) \times \widehat{\mathbf{W}}_h$ such that:

$$\begin{aligned}
&\rho^f(\partial_t \mathbf{u}_h, \mathbf{v}_h)_{\Omega^f(t)} + a^f(\mathbf{u}_h, \mathbf{v}_h) + b(p_h, \mathbf{v}_h) - b(q_h, \mathbf{u}_h) + c(\mathbf{u}_h, \mathbf{u}_h, \mathbf{v}_h) \\
&+ \rho^s(\partial_{tt}\widehat{\mathbf{d}}_h, \widehat{\mathbf{w}}_h)_{\widehat{\Omega}^s} + a^s(\widehat{\mathbf{d}}_h, \widehat{\mathbf{w}}_h) + s_h(\mathbf{u}_h, p_h; \mathbf{v}_h, q_h) + g_h(\mathbf{u}_h, \mathbf{v}_h) \\
&- (\alpha \mathbf{T}^f(\mathbf{u}_h, p_h)\mathbf{n}^f + (1-\alpha)\mathbf{T}^s(\mathbf{d}_h)\mathbf{n}^f, \mathbf{v}_h - \mathbf{w}_h)_{\Sigma(t)} \\
&- (\mathbf{u}_h - \dot{\mathbf{d}}_h, \alpha \mathbf{T}^f(\mathbf{v}_h, -q_h)\mathbf{n}^f + (1-\alpha)\mathbf{T}^s(\mathbf{w}_h)\mathbf{n}^f)_{\Sigma(t)} \\
&+ \frac{\gamma_\Sigma \mu^f}{h}(\mathbf{u}_h - \dot{\mathbf{d}}_h, \mathbf{v}_h - \mathbf{w}_h)_{\Sigma(t)} = (\mathbf{f}^f, \mathbf{v}_h)_{\Omega^f(t)} + (\widehat{\mathbf{f}}^s, \widehat{\mathbf{w}}_h)_{\widehat{\Omega}^s},
\end{aligned} \tag{4}$$

$\forall\, (\mathbf{v}_h(t), q_h(t), \widehat{\mathbf{w}}_h) \in \mathbf{V}_h(t) \times Q_h(t) \times \widehat{\mathbf{W}}_h$.

We have indicated with

$$a^f(\mathbf{u}, \mathbf{v}) = 2\mu^f(\mathbf{D}(\mathbf{u}), \nabla \mathbf{v})_{\Omega^f(t)}, \qquad a^s(\widehat{\mathbf{d}}, \widehat{\mathbf{w}}) = (\widehat{\mathbf{T}}^s(\widehat{\mathbf{d}}), \nabla \widehat{\mathbf{w}})_{\widehat{\Omega}_s},$$
$$b(p, \mathbf{v}) = -(p, \nabla \cdot \mathbf{v})_{\Omega^f(t)}, \qquad c(\mathbf{z}, \mathbf{u}, \mathbf{v}) = \rho^f(\mathbf{z} \cdot \nabla \mathbf{u}, \mathbf{v})_{\Omega^f(t)},$$

and $s_h(\mathbf{u}_h, p_h; \mathbf{v}_h, q_h)$ is the bilinear form that collects the stabilization terms for the Navier-Stokes equation and ensures the discrete $inf - sup$ condition and the control og the velocity oscillations at high Reynolds number. In this work, we employ the *continuous interior penalty*, see e.g. [17]. On $\mathcal{F}_{\mathcal{G},h}(t)$ we have applied the ghost penalty stabilization term defined as

$$g_h(\mathbf{u}_h, \mathbf{v}_h) = \gamma_g \sum_{F \in \mathcal{F}_{\mathcal{G},h}(t)} \mu^f h_F \int_F [\![\nabla \mathbf{u}_h]\!]\, \mathbf{n} \cdot [\![\nabla \mathbf{v}_h]\!]\, \mathbf{n},$$

where $\gamma_g > 0$, $[\![\mathbf{S}]\!] = \mathbf{S}^+ - \mathbf{S}^-$ is the trace operator representing the jump of a tensor-value function $\mathbf{S}$ across the interface between the elements K^+ and K^-, while on the faces belonging to the fluid-structure interface $\Sigma(t)$ we have weakly imposed the continuity of the velocity via a Discontinuous Galerkin approach. In particular we have employed the symmetric interior penalty method, see e.g. [6, 22, 23], with $\gamma_\Sigma > 0$ the penalty parameter and $\alpha \in [0, 1]$.

Regarding the discretization in time, we employ the implicit Euler scheme for both fluid and solid problems with time step Δt. Note that the fluid integrals appearing in the formulation (4) should be integrated on the current configuration which is itself an unknown. To handle this issue, we use a first order extrapolation in time for the fluid domain. The resulting fully-discrete formulation represents a non-linear system of equations which is linearized with an inexact Newton algorithm, see [56].

3 Contact model in the unfitted framework

In this section, we consider the numerical framework presented in Section 2 in the case where both fluid-structure interaction and contact occur. We first introduce the contact model and then we consider XFEM/DG formulation for the FSI problem with contact. The contact model we present is a *master-slave* approach, i.e. the contact conditions are applied only to the *slave* body which undergoes the contact exerted by the *master* body. Moreover, we assume that the contact is frictionless, i.e. the tangential component of the contact traction is zero, by prescribing only the non-penetration condition.

3.1 Penalty contact model

To ease the presentation of the contact model, we consider two bodies described by the domains $\Omega^s(t)$ and $\Omega^m(t)$, where the *slave* body $\Omega^s(t)$ is subject to the elastodynamics equation, while the *master* body $\Omega^m(t)$ is considered rigid and fixed in time, i.e. $\Omega^m(t) = \Omega^m$. In particular we assume that the boundary of Ω^m is modeled as a rigid plane Γ^w characterized by a given unit normal $\mathbf{n}^w$ pointing inwards Ω^m. We denote by $\mathbf{n}^s(t)$ and $\mathbf{n}^m$ the outward unit normals of $\Omega^s(t)$ and Ω^m, respectively, noticing that $\mathbf{n}^m = -\mathbf{n}^w$.

We introduce a decomposition into normal and tangential components in the frame of reference of the rigid plane Γ^w for a vector field $\mathbf{v}$ and for a stress tensor $\mathbf{T}$:

$$\mathbf{v} = v_n \mathbf{n}^w + \mathbf{v_t}, \quad \mathbf{Tn} = T_n \mathbf{n}^w + \mathbf{T_t},$$

where T_n and v_n stands for the normal components, i.e.:

$$v_n = \mathbf{v} \cdot \mathbf{n}^w, \qquad T_n = \mathbf{Tn} \cdot \mathbf{n}^w.$$

We introduce $\Delta : \partial\Omega^s(t) \to \mathbb{R}$ as the *current gap* function, defined as the distance from a point $\mathbf{x}^s$ of the boundary of the slave body to the plane Γ^w, i.e. the length of the projection on the rigid plane Γ^w of any point of the current solid position, namely,

$$\Delta = (\mathbf{x}^w - \mathbf{x}^s) \cdot \mathbf{n}^w, \quad \forall \mathbf{x}^s \in \partial\Omega^s(t),$$

where $\mathbf{x}^w$ is a generic point of Γ^w, see Figure 4. We also indicate by $\Gamma_C^s(t)$ the portion of $\partial\Omega^s(t)$ where the contact occurs.

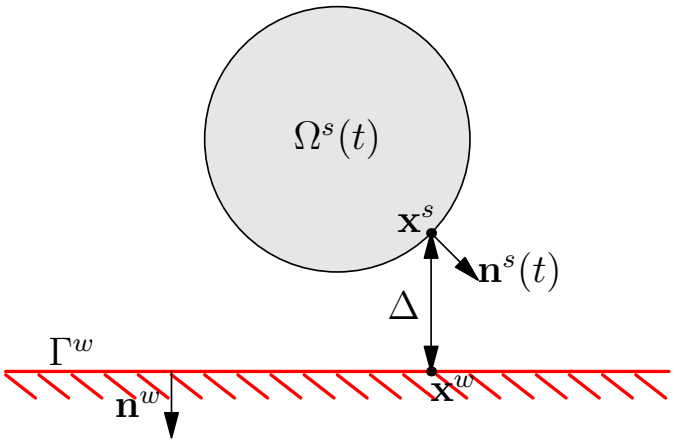

Figure 4: Sketch of the flexible body $\Omega^s(t)$ and the rigid wall Γ^w (red).

For an elastic body the unilateral frictionless contact constraints in a master-slave approach are formulated as follows:

$$\Delta \geq 0, \quad \lambda \leq 0, \quad \lambda\Delta = 0, \qquad \text{on } \partial\Omega^s(t), \tag{5a}$$

$$\boldsymbol{\varphi} = \mathbf{0}, \qquad \text{on } \partial\Omega^s(t), \tag{5b}$$

where $\lambda = T_n^s$ and $\boldsymbol{\varphi} = \mathbf{T}_\mathbf{t}^s$ are the normal and tangential components of the *contact traction*, respectively.

The first inequality in equation (5a) ensures that the solid does not cross the plane Γ^w; the second one describes that the normal component of the contact traction is zero (in absence of contact) or negative (during contact), i.e. it acts as a compression for the slave body; the third condition is the complementarity condition that guarantees that at least one of the two constraints is zero. No constraint is imposed along the tangential direction, so the contact is friction-less. Note that these conditions are the classical unilateral contact conditions (Karush-Kuhn-Tucker conditions) in case of contact mechanics, see e.g. [40, 57, 25, 3]).

Following [26], for an arbitrary positive function γ_C defined on $\partial\Omega^s(t)$, the conditions of equation (5) can be approximated in a single non-linear relation:

$$\lambda = -\gamma_C[-\Delta]_{\mathbb{R}^+}, \tag{6}$$

where the notation $[\cdot]_{\mathbb{R}^+}$ stands for the projection onto $\mathbb{R}^+$, namely,

$$[x]_{\mathbb{R}^+} = \frac{1}{2}\left(|x| + x\right) = \begin{cases} x, & x > 0, \\ 0, & x \leq 0. \end{cases}$$

Remark 1 *Notice that the relation given by equation* (6) *is not equivalent to the contact conditions of equation* (5) *and will yield a non-consistent formulation. In fact, a consistent formulation can be recovered replacing relation* (6) *with the following one,*

$$\lambda = -\gamma_C[-\Delta - \frac{1}{\gamma_C}\lambda]_{\mathbb{R}^+},$$

see e.g. [25, 24, 27, 28].

In the variational setting, the contact conditions lead to the introduction of the traction λ on the boundary of the slave body. In particular, the relation (6) leads to the following variational penalty contact term:

$$-\int_{\partial\Omega^s(t)} \lambda w_n = +\gamma_C \int_{\partial\Omega^s(t)} [-\Delta]_{\mathbb{R}^+} w_n = -\gamma_C \int_{\Gamma_C^s(t)} \Delta w_n. \tag{7}$$

3.2 XFEM/DG formulation for FSI-contact model

In what follows, we consider a slave structure $\Omega^s(t)$ fully immersed in a fluid $\Omega^f(t)$ and a master structure $\Omega^m(t)$, by assuming that the slave body $\Omega^s(t)$ is subject to the elastodynamics equation while the master one $\Omega^m(t)$ is considered rigid, fixed in time and its boundary coincides with a boundary of the fluid domain indicated with Γ^w, see Figure 5. We indicate with $\Sigma^s(t)$ the fluid-structure interface between the fluid and the slave body. Notice that $\Sigma^s(t) = \partial\Omega^s(t)$.

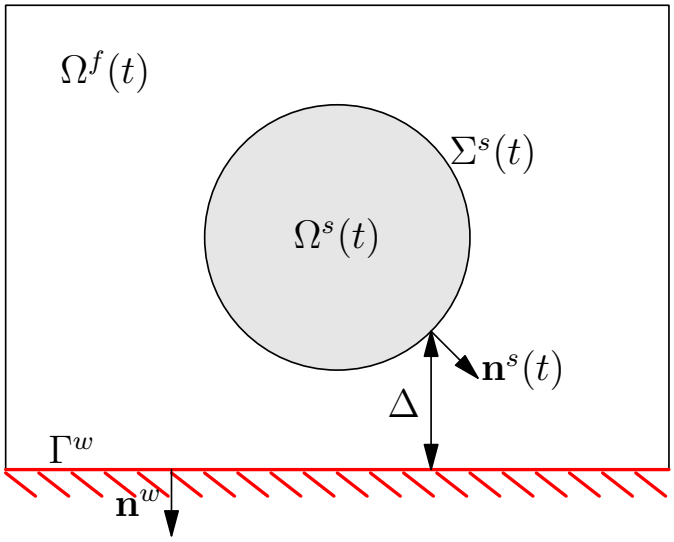

Figure 5: Sketch of the fluid and structure domains $\Omega^f(t)$ (white) and $\Omega^s(t)$ (grey) and the boundary of the master body Γ^w (red).

The coupling between the FSI problem introduced in Section 2.1 with the contact model presented in Section 3.1 leads to the following problem:

Find, for any $t \in (0,T]$, the fluid velocity $\mathbf{u}(t) : \Omega^f(t) \to \mathbb{R}^d$, the fluid pressure $p(t) : \Omega^f(t) \to \mathbb{R}$, the solid displacement $\widehat{\mathbf{d}}^s(t) : \widehat{\Omega}^s \to \mathbb{R}^d$, such that:

$$\begin{cases} \rho^f \partial_t \mathbf{u} + \rho^f \mathbf{u} \cdot \nabla \mathbf{u} - \nabla \cdot \mathbf{T}^f(\mathbf{u}, p) = \mathbf{f}^f, & \text{in } \Omega^f(t), \\ \nabla \cdot \mathbf{u} = 0, & \text{in } \Omega^f(t), \\ \mathbf{u} = \mathbf{0}, & \text{on } \Gamma^f \cup \Gamma^w; \end{cases} \tag{8}$$

$$\rho^s \partial_{tt} \widehat{\mathbf{d}}^s - \nabla \cdot \widehat{\mathbf{T}}^s(\widehat{\mathbf{d}}^s) = \widehat{\mathbf{f}}^s, \quad \text{in } \widehat{\Omega}^s; \tag{9}$$

$$\begin{cases} \mathbf{u} = \dot{\mathbf{d}}^s, & \text{on } \Sigma^s(t), \\ \mathbf{T}^f(\mathbf{u}, p)\mathbf{n} = \mathbf{T}^s(\mathbf{d}^s)\mathbf{n}, & \text{on } \Sigma^s(t), \\ \Delta \geq 0, \quad \lambda \leq 0, \quad \lambda \Delta = 0, & \text{on } \Sigma^s(t), \\ \boldsymbol{\varphi} = \mathbf{0}, & \text{on } \Sigma^s(t). \end{cases} \tag{10}$$

By using the same discrete functional spaces for the approximation of the fluid velocity, fluid pressure and solid displacement introduced in Section 2.2, and by applying the penalty contact model given by equation (5), we write the semi-discrete formulation of the problem given by the equations (8)-(10) as follows:
For any $t > 0$, find $(\mathbf{u}_h(t), p_h(t), \widehat{\mathbf{d}}_h^s(t)) \in \mathbf{V}_h(t) \times Q_h(t) \times \widehat{\mathbf{W}}_h^s$ such that:

$$\begin{aligned} &\rho^f(\partial_t \mathbf{u}_h, \mathbf{v}_h)_{\Omega^f(t)} + a^f(\mathbf{u}_h, \mathbf{v}_h) + b(p_h, \mathbf{v}_h) - b(q_h, \mathbf{u}_h) + c(\mathbf{u}_h, \mathbf{u}_h, \mathbf{v}_h) \\ &+ \rho^s(\partial_{tt} \widehat{\mathbf{d}}_h^s, \widehat{\mathbf{w}}_h^s)_{\widehat{\Omega}^s} + a^s(\widehat{\mathbf{d}}_h^s, \widehat{\mathbf{w}}_h^s) + s_h(\mathbf{u}_h, p_h; \mathbf{v}_h, q_h) + g_h(\mathbf{u}_h, \mathbf{v}_h) \\ &- (\alpha \mathbf{T}^f(\mathbf{u}_h, p_h)\mathbf{n}^f + (1-\alpha)\mathbf{T}^s(\mathbf{d}_h^s)\mathbf{n}^f, \mathbf{v}_h - \mathbf{w}_h^s)_{\Sigma^s(t)} \\ &- (\mathbf{u}_h - \dot{\mathbf{d}}_h^s, \alpha \mathbf{T}^f(\mathbf{v}_h, -q_h)\mathbf{n}^f + (1-\alpha)\mathbf{T}^s(\mathbf{w}_h^s)\mathbf{n}^f)_{\Sigma^s(t)} \\ &+ \frac{\gamma_\Sigma \mu^f}{h}(\mathbf{u}_h - \dot{\mathbf{d}}_h^s, \mathbf{v}_h - \mathbf{w}_h^s)_{\Sigma^s(t)} \\ &+ \frac{\gamma_{C_0}}{h} \int_{\Sigma^s(t)} [-\Delta]_{\mathbb{R}^+} w_{n,h}^s = (\mathbf{f}^f, \mathbf{v}_h)_{\Omega^f} + (\widehat{\mathbf{f}}^s, \widehat{\mathbf{w}}_h)_{\widehat{\Omega}^s}, \end{aligned} \tag{11}$$

$\forall\ (\mathbf{v}_h(t), q_h(t), \widehat{\mathbf{w}}_h) \in \mathbf{V}_h(t) \times Q_h(t) \times \widehat{\mathbf{W}}_h^s$, where $\gamma_C = \frac{\gamma_{C_0}}{h}$ and $\gamma_{C_0} > 0$ is a positive penalty parameter.

Notice that the contact term in (11) is non null only when the argument of the projection function is positive, i.e. only when contact happens. In this case we can define a subset $\Gamma_C^s(t) \subset \partial\Omega^s(t)$ which identifies the contact surface:

$$\Gamma_C^s(t) = \{\mathbf{x} \in \partial\Omega^s(t) : \Delta < 0\}.$$

Remark 2 *For practical purposes, it may be convenient to relax the contact conditions by introducing a small parameter $\varepsilon > 0$, so that we consider the slave body comes into contact with the master one only if the distance between them is lower than ε, i.e $\Delta < \varepsilon$. This choice allows to avoid penetration between the bodies during the iterative*

procedure in the numerical solver. Hence, we can reformulate the contact condition as follows:

$$\begin{aligned} &\Delta - \varepsilon \geq 0, \quad \lambda \leq 0, \quad \lambda(\Delta - \varepsilon) = 0, && \text{on } \partial\Omega^s(t), \\ &\boldsymbol{\varphi} = \mathbf{0}, && \text{on } \partial\Omega^s(t), \end{aligned}$$

and the variational penalty contact term given by equation (7) *becomes:*

$$-\int_{\partial\Omega^s(t)} \lambda w_n^s = +\gamma_C \int_{\partial\Omega^s(t)} [\varepsilon - \Delta]_{\mathbb{R}^+} w_n^s = -\gamma_C \int_{\Gamma_C^s(t)} (\varepsilon - \Delta)\, w_n^s.$$

By applying the time discretization as described in Section 2.2, the fully-discrete formulation reads as follows:
For any $n = 0, \ldots, \frac{T}{\Delta t} - 1$, $T > 0$, find $(\mathbf{u}_h^{n+1}, p_h^{n+1}, \widehat{\mathbf{d}}_h^{s,n+1}) \in \mathbf{V}_h^{n+1} \times Q_h^{n+1} \times \widehat{\mathbf{W}}_h^s$ such that:

$$\begin{aligned} &\frac{\rho^f}{\Delta t}\left(\mathbf{u}_h^{n+1}, \mathbf{v}_h\right)_{\Omega^{f,n}} + a^f\left(\mathbf{u}_h^{n+1}, \mathbf{v}_h\right) + b\left(p_h^{n+1}, \mathbf{v}_h\right) - b\left(q_h, \mathbf{u}_h^{n+1}\right) \\ &+ c\left(\mathbf{u}_h^{n+1}, \mathbf{u}_h^{n+1}, \mathbf{v}_h\right) + \frac{\rho^s}{\Delta t^2}\left(\widehat{\mathbf{d}}_h^{s,n+1}, \widehat{\mathbf{w}}_h^s\right)_{\widehat{\Omega}^s} + a^s\left(\widehat{\mathbf{d}}_h^{s,n+1}, \widehat{\mathbf{w}}_h^s\right) \\ &+ s_h\left(\mathbf{u}_h^{n+1}, p_h^{n+1}; \mathbf{v}_h, q_h\right) + g_h\left(\mathbf{u}_h^{n+1}, \mathbf{v}_h\right) \\ &- \left(\alpha \mathbf{T}^f(\mathbf{u}_h^{n+1}, p_h^{n+1})\mathbf{n}^f + (1-\alpha)\mathbf{T}^s(\mathbf{d}_h^s)\mathbf{n}^f, \mathbf{v}_h - \mathbf{w}_h^s\right)_{\Sigma^{s,n}} \\ &- \left(\mathbf{u}_h^{n+1} - \frac{\mathbf{d}_h^{s,n+1}}{\Delta t}, \alpha \mathbf{T}^f(\mathbf{v}_h, -q_h)\mathbf{n}^f + (1-\alpha)\mathbf{T}^s(\mathbf{w}_h^s)\mathbf{n}^f\right)_{\Sigma^{s,n}} \\ &+ \frac{\gamma_\Sigma \mu^f}{h}\left(\mathbf{u}_h^{n+1} - \frac{\mathbf{d}_h^{s,n+1}}{\Delta t}, \mathbf{v}_h - \mathbf{w}_h^s\right)_{\Sigma^{s,n}} + \frac{\gamma_{C_0}}{h}\int_{\Sigma^{s,n}} [-\Delta^{n+1}]_{\mathbb{R}^+} w_{n,h}^s \\ &= \frac{\rho^f}{\Delta t}\left(\mathbf{u}_h^n, \mathbf{v}_h\right)_{\Omega^{f,n}} + \frac{2\rho^s}{\Delta t^2}\left(\widehat{\mathbf{d}}_h^{s,n}, \widehat{\mathbf{w}}_h^s\right)_{\widehat{\Omega}^s} - \frac{\rho^s}{\Delta t^2}\left(\widehat{\mathbf{d}}_h^{s,n-1}, \widehat{\mathbf{w}}_h^s\right)_{\widehat{\Omega}^s} \\ &+ \left(\frac{\mathbf{d}_h^{s,n}}{\Delta t}, \alpha \mathbf{T}^f(\mathbf{v}_h, -q_h)\mathbf{n}^f + (1-\alpha)\mathbf{T}^s(\mathbf{w}_h^s)\mathbf{n}^f\right)_{\Sigma^{s,n}} \\ &- \frac{\gamma_\Sigma \mu^f}{h}\left(\frac{\mathbf{d}_h^{s,n}}{\Delta t}, \mathbf{v}_h - \mathbf{w}_h^s\right)_{\Sigma^{s,n}} + \left(\mathbf{f}^f, \mathbf{v}_h\right)_{\Omega^{f,n}} + \left(\widehat{\mathbf{f}}^s, \widehat{\mathbf{w}}_h^s\right)_{\widehat{\Omega}^s}, \end{aligned}$$

$\forall\, (\mathbf{v}_h, q_h, \widehat{\mathbf{w}}_h) \in \mathbf{V}_h^{n+1} \times Q_h^{n+1} \times \widehat{\mathbf{W}}_h^s$.

To extend the formulation presented above for the case of contact between flexible bodies, i.e. when also $\Omega^m(t)$ is subject to the elastodynamics equation, we have to generalize the definition of the current gap function Δ. First, we introduce the projection map $\Pi : \partial\Omega^s(t) \to \partial\Omega^m(t)$ that, given a point on the boundary of the slave body $\mathbf{x}^s \in \partial\Omega^s(t)$, returns its projection on the boundary of the master domain. The current gap function Δ is now given by:

$$\Delta = \left(\Pi\left(\mathbf{x}^s\right) - \mathbf{x}^s\right) \cdot \widetilde{\mathbf{n}}^w, \quad \forall \mathbf{x}^s \in \partial\Omega^s(t),$$

where $\widetilde{\mathbf{n}}^w$ is the unit normal pointing inwards $\Omega^m(t)$ of $\Pi\left(\mathbf{x}^s\right)$, i.e. $\widetilde{\mathbf{n}}^w = \mathbf{n}^w \circ \Pi(\mathbf{x}^s)$. Notice that, indicating by $\mathbf{x}^m = \Pi(\mathbf{x}^s)$, we have $\mathbf{n}^m\left(\mathbf{x}^m\right) = -\widetilde{\mathbf{n}}^w$.

The fully-discrete formulation in the case of two elastic bodies reads as follows: For any $n = 0, \ldots, \frac{T}{\Delta t} - 1$, $T > 0$, find $(\mathbf{u}_h^{n+1}, p_h^{n+1}, \widehat{\mathbf{d}}_h^{s,n+1}, \widehat{\mathbf{d}}_h^{m,n+1}) \in \mathbf{V}_h^{n+1} \times Q_h^{n+1} \times \widehat{\mathbf{W}}_h^s \times \widehat{\mathbf{W}}_h^m$ such that:

$$
\begin{aligned}
&\frac{\rho^f}{\Delta t}\left(\mathbf{u}_h^{n+1}, \mathbf{v}_h\right)_{\Omega^{f,n}} + a^f\left(\mathbf{u}_h^{n+1}, \mathbf{v}_h\right) + b\left(p_h^{n+1}, \mathbf{v}_h\right) - b\left(q_h, \mathbf{u}_h^{n+1}\right) \\
&+ c\left(\mathbf{u}_h^{n+1}, \mathbf{u}_h^{n+1}, \mathbf{v}_h\right) + \sum_{i=s,m}\left(\frac{\rho^i}{\Delta t^2}\left(\widehat{\mathbf{d}}_h^{i,n+1}, \widehat{\mathbf{w}}_h^i\right)_{\widehat{\Omega}^i} + a^i\left(\widehat{\mathbf{d}}_h^{i,n+1}, \widehat{\mathbf{w}}_h^i\right)\right) \\
&+ s_h\left(\mathbf{u}_h^{n+1}, p_h^{n+1}; \mathbf{v}_h, q_h\right) + g_h\left(\mathbf{u}_h^{n+1}, \mathbf{v}_h\right) \\
&- \sum_{i=s,m}\left(\alpha\mathbf{T}^f(\mathbf{u}_h^{n+1}, p_h^{n+1})\mathbf{n}^f + (1-\alpha)\mathbf{T}^i(\mathbf{d}_h^i)\mathbf{n}^f, \mathbf{v}_h - \mathbf{w}_h^i\right)_{\Sigma^{i,n}} \\
&- \sum_{i=s,m}\left(\mathbf{u}_h^{n+1} - \frac{\mathbf{d}_h^{i,n+1}}{\Delta t}, \alpha\mathbf{T}^f(\mathbf{v}_h, -q_h)\mathbf{n}^f + (1-\alpha)\mathbf{T}^i(\mathbf{w}_h^i)\mathbf{n}^f\right)_{\Sigma^{i,n}} \\
&+ \sum_{i=s,m}\frac{\gamma_\Sigma\mu^f}{h}\left(\mathbf{u}_h^{n+1} - \frac{\mathbf{d}_h^{i,n+1}}{\Delta t}, \mathbf{v}_h - \mathbf{w}_h^i\right)_{\Sigma^{i,n}} \\
&+ \frac{\gamma_{C_0}}{h}\int_{\Sigma^{s,n}}\left[-\Delta^{n+1}\right]_{\mathbb{R}^+}\left(w_{n,h}^s - w_{n,h}^m\right) \\
&= \frac{\rho^f}{\Delta t}\left(\mathbf{u}_h^n, \mathbf{v}_h\right)_{\Omega^{f,n}} + \sum_{i=s,m}\left(\frac{2\rho^i}{\Delta t^2}\left(\widehat{\mathbf{d}}_h^{i,n}, \widehat{\mathbf{w}}_h^i\right)_{\widehat{\Omega}^i} - \frac{\rho^i}{\Delta t^2}\left(\widehat{\mathbf{d}}_h^{i,n-1}, \widehat{\mathbf{w}}_h^i\right)_{\widehat{\Omega}^i}\right) \\
&+ \sum_{i=s,m}\left(\frac{\mathbf{d}_h^{i,n}}{\Delta t}, \alpha\mathbf{T}^f(\mathbf{v}_h, -q_h)\mathbf{n}^f + (1-\alpha)\mathbf{T}^i(\mathbf{w}_h^i)\mathbf{n}^f\right)_{\Sigma^{s,n}} \\
&- \sum_{i=s,m}\frac{\gamma_\Sigma\mu^f}{h}\left(\frac{\mathbf{d}_h^{i,n}}{\Delta t}, \mathbf{v}_h - \mathbf{w}_h^i\right)_{\Sigma^{i,n}} + \left(\mathbf{f}^f, \mathbf{v}_h\right)_{\Omega^{f,n}} + \sum_{i=s,m}\left(\widehat{\mathbf{f}}^i, \widehat{\mathbf{w}}_h^i\right)_{\widehat{\Omega}^i},
\end{aligned}
$$

$\forall\,(\mathbf{v}_h, q_h, \widehat{\mathbf{w}}_h) \in \mathbf{V}_h^{n+1} \times Q_h^{n+1} \times \widehat{\mathbf{W}}_h^s \times \widehat{\mathbf{W}}_h^m$.

4 Numerical examples

In this section, we present three numerical examples concerning the penalty contact model for FSI presented in Section 3. We consider the case of a falling elastic ball coming in contact with, first, a virtual barrier immersed in the fluid, then with a rigid ground, and finally with an elastic ground.

In these tests, we set the parameter $\alpha = 1$ to ensure numerical stability of the FSI problem, see e.g. [4]. At each time step, we treat the non-linearities via the inexact Newton method presented in [56] and the resulting linear system is solved monolithically via the GMRES iterative solver with a block Gauss-Seidel preconditioner, see [60].

The XFEM/DG approach has been developed in the finite elements library LifeV [41]. For further details on the implementation, see [61].

4.1 Free fall of an elastic ball on a virtual barrier

To test the proposed contact algorithm implemented in the XFEM/DG method, we consider a 2D elastic ball immersed in a fluid falling towards a planar rigid ground, see Figure 6. The solid domain $\widehat{\Omega}^s$ is a disk of radius $r = 4\,cm$ with center located at $(0, 10)\,cm$. The solid is fully immersed in a fluid domain $\Omega^f(t)$ and falls towards the boundary of the fluid domain $\Gamma^w = \{(x, y) \in \mathbb{R}^2 : y = 0\}$, due to a gravity field $\widehat{\mathbf{f}}^s = (0, -10^3)\,cm/s^2$. We denote with $\Omega = (-10, 10) \times (0, 15)\,cm^2$ the domain given by the union of the solid and fluid domains. Initially both the fluid and the solid are at rest. On the boundary Γ^w, we apply a zero velocity condition, while on the other part of the boundary fluid domain we apply a homogeneous Neumann condition.

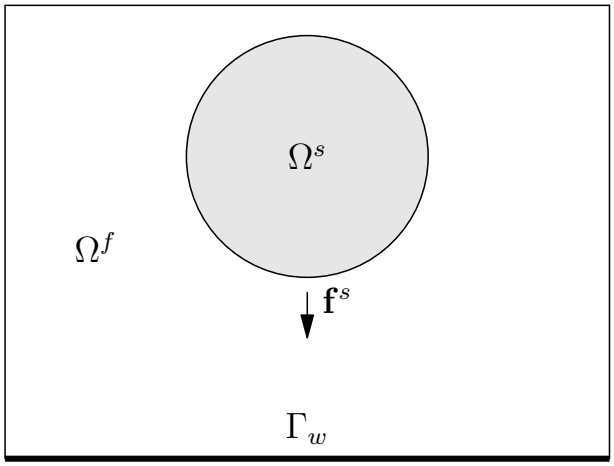

Figure 6: The ball (grey) is immersed in the fluid domain (white) and Γ^w is the bottom boundary of the fluid domain. "Virtual barrier" test case.

For the solid, we use the Saint Venant-Kirchhoff material law:

$$\widehat{\mathbf{T}}^s = 2\mu^s\mathbf{E} + \lambda^s \mathrm{tr}(\mathbf{E})\mathbf{I},$$

where $\mathbf{E} = \frac{1}{2}(\mathbf{F}^T\mathbf{F} - \mathbf{I})$ is the Green-Lagrange strain tensor. For the physical parameters, we use the Lamé parameters $\mu^s = 2 \cdot 10^6\, dyne/cm$, $\lambda^s = 8 \cdot 10^6\, dyne/cm$, the fluid dynamic viscosity $\mu^f = 10^{-2}\, dyne \cdot s$, and the fluid and solid densities $\rho^s = \rho^f = 1\, g\, cm^{-2}$.

Due to the low Reynolds number and the symmetry of the problem, we expect to obtain a symmetric solution with respect to the vertical axis. For this reason, we decide to simulate only half of the domain to reduce the computational cost, by imposing symmetry boundary conditions on the plane of symmetry, i.e. $\widehat{\mathbf{d}}^s \cdot \widehat{\mathbf{n}} = 0$ and $\mathbf{u} \cdot \mathbf{n} = 0$ for the solid and fluid respectively, see Figure 7 (left).

We use a non-uniform isotropic background mesh with a space resolution of $0.5\,cm$ in the upper part of the domain and of $0.1\,cm$ in the proximity of the wall Γ^w. For the solid mesh we use a uniform isotropic grid of size $0.1\,cm$. In the Figure 7 (right), we sketch the background and foreground meshes used in the simulations. For the numerical setting, we choose $\gamma_g = 1$, $\gamma_\Sigma = 10^5$, $\gamma_{C_0} = 10^8$ and $\Delta t = 10^{-3}\,s$. Moreover, to model the virtual barrier we set $\varepsilon = 3\,cm$, see Remark 2.

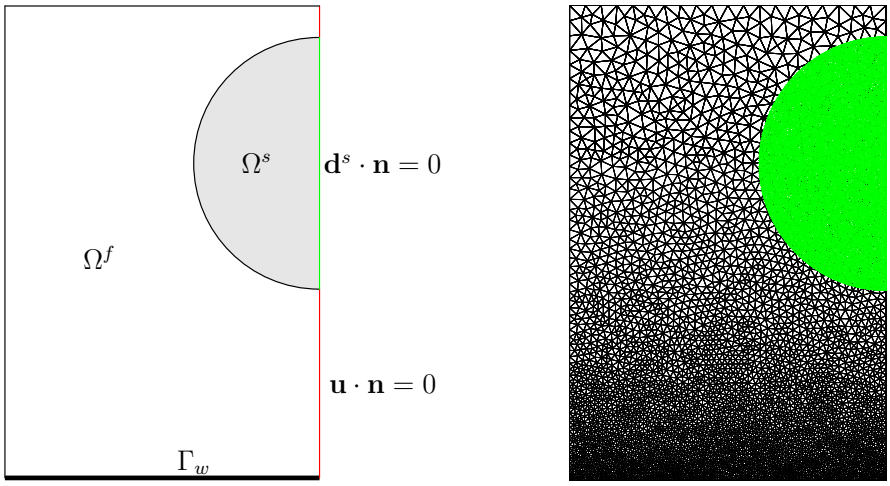

Figure 7: Sketch of the reduced domain (left) and the corresponding mesh (right). "Virtual barrier" test case.

In Figure 8, we plot the minimum distance d_{min} between Γ^w and the ball over time, the top/bottom distance $d_{\text{max}} - d_{\text{min}}$ of the ball over time, the velocity and acceleration related to the point at minimum distance between the ball and Γ^w. We observe that the solid is pulled down by the gravity until it reaches the virtual barrier at time $0.111\,s$.

Since the plane is non physical, the ball arrives in contact without any previous compression. Then, at time $0.126\,s$, the ball is released from contact and it reaches its maximum height at time $0.182\,s$, i.e. $d_{\text{min}} \approx 3.8\,cm$. From this point the ball falls down again due to gravity.

During contact, the maximum violation of the non-penetration condition below ε corresponds to about 1% of the local mesh size.

From Figure 8 (bottom left), we observe that the compression that interests the ball during contact causes the activation of some vibration modes in the structure that are then damped. Note that the strong variations in the velocity u_y corresponds to the collision and release of the ball with the virtual barrier, see Figure 8 (top right), and the peaks in the acceleration a_y are due to the discontinuities in the velocity, see Figure 8 (bottom right).

In Figure 9, we plot the vertical solid displacement isolines when we have the maximum violation of the non-penetration condition.

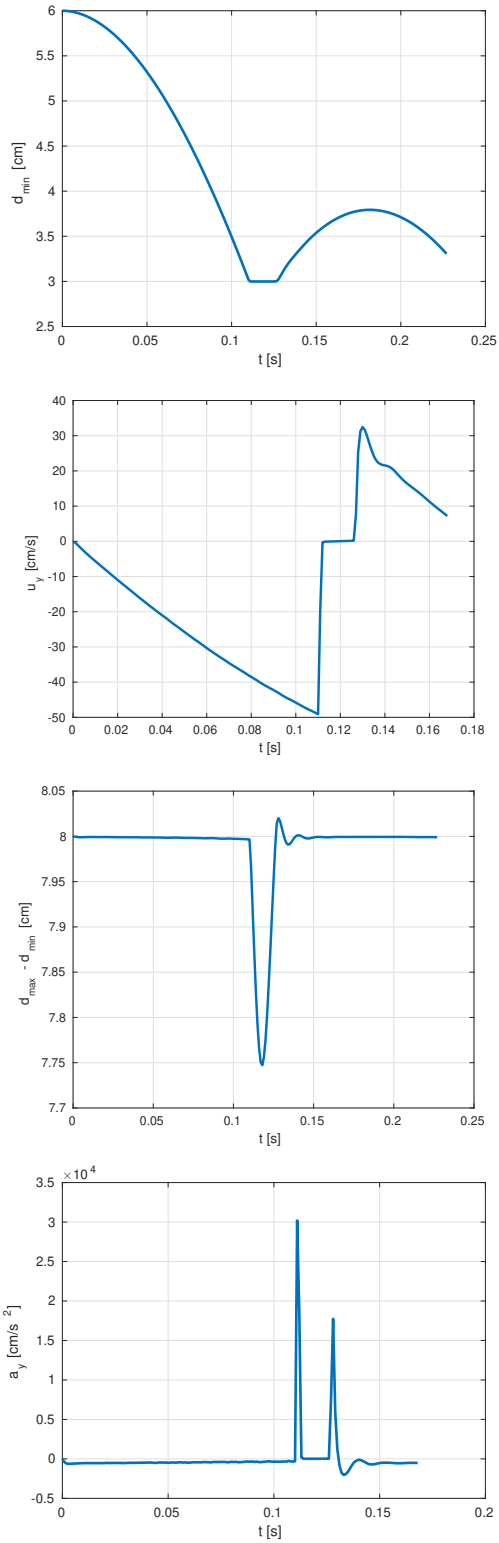

Figure 8: Top left: minimum distance from Γ^w of the ball over time. Bottom left: top/bottom distance of the ball over time. Top right: velocity over time of the solid point at the minimum distance from Γ^w. Bottom right: acceleration over time of the solid point at minimum distance from Γ^w. "Virtual barrier" test case.

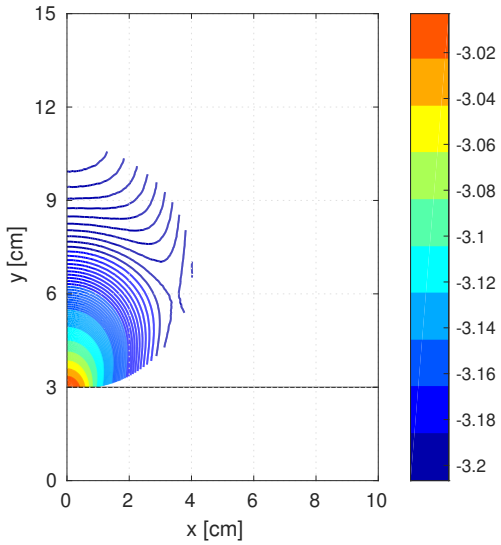

Figure 9: Isolines of the solid displacement in the y direction at the time $0.115\,s$ corresponding to the maximum violation of the non-penetration condition. "Virtual barrier" test case.

4.2 Free fall of an elastic ball on a rigid ground

In this examples, we consider the configuration and parameters use for the test in Section 4.1. The difference is that we set $\varepsilon = h$, see Remark 2, to model the contact with the rigid ground.

In Figure 10, we plot the minimum distance d_{min} between the ball and the ground, and the top/bottom distance $d_{\text{max}} - d_{\text{min}}$ of the ball. In this case when the ball approaches Γ^w, as opposed to the virtual barrier, the ball is already compressed due to the high fluid pressure generated by the presence of Γ^w.

In Figure 11, we plot the vorticity isolines and fluid velocity vectors at $t = 0.177\,s$, i.e. when the ball comes into contact with the ground.

To investigate the influence of the time step, we perform the same simulation with $\Delta t = 2 \cdot 10^{-3}\,s$ and $\Delta t = 2 \cdot 10^{-4}\,s$. Table 1 shows the contact time and the time at which the ball reaches the maximum elevation after the rebound for the three time steps used. We observe that the time increases by refining the time step. For the higher time step, i.e. $\Delta t = 2 \cdot 10^{-3}\,s$, we have noticed that the ball drops out of the fluid domain at the second bouncing with the rigid ground. This means that the time step is not sufficiently fine to resolve correctly the contact dynamics. For the three time steps, we notice that the maximum height reached after the rebound increases slightly, as time step decreases. From the greater to the finer time step the maximum height increases of about 50% the resolution grid in that region.

In Figure 12, we show the top/bottom distance for the smaller and higher time step. We notice that, for the finer time step, the peaks are delayed in time and with a greater

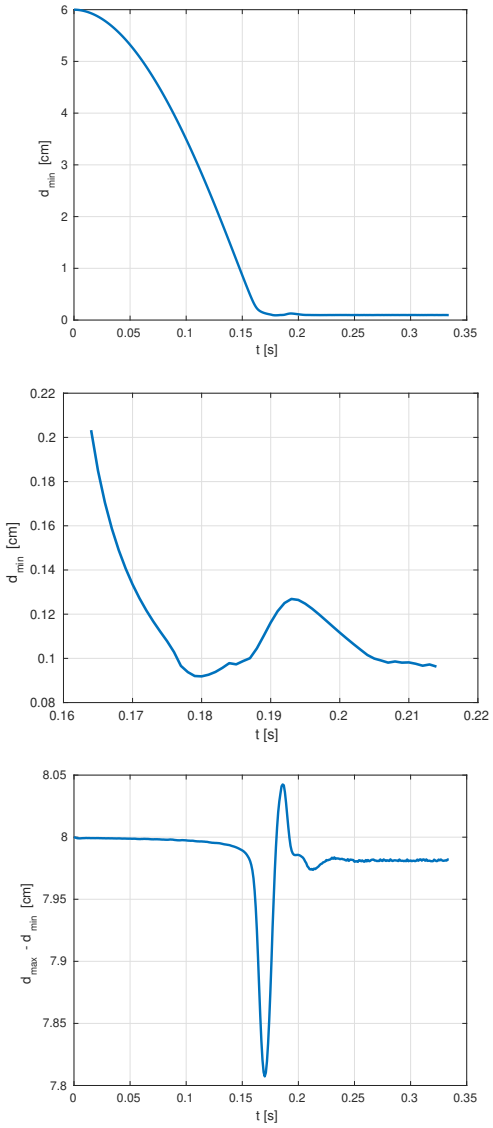

Figure 10: Top left: minimum distance from Γ^w of the ball over time. Top right: zoom of the minimum distance during the contact. Bottom: top/bottom distance of the ball over time. Results for time step $\Delta t = 10^{-3}\ s$. "Rigid ground" test case.

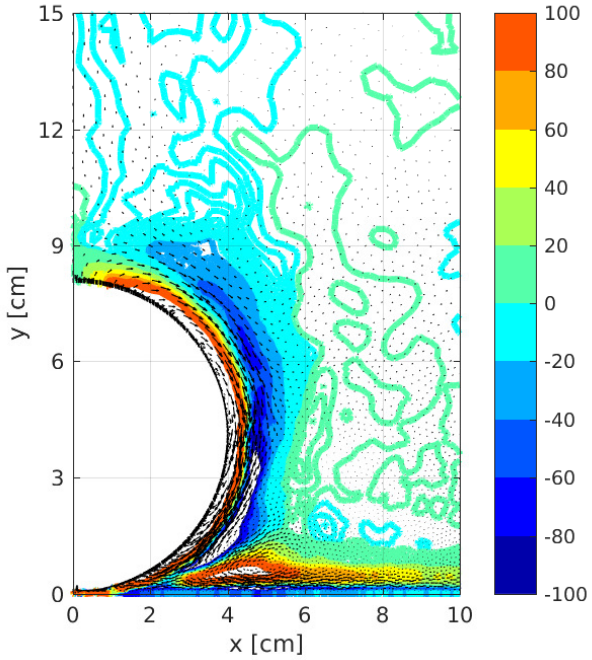

Figure 11: Vorticity isolines and fluid velocity vectors at the instance of contact $t = 0.177\,s$. Results for time step $\Delta t = 10^{-3}\,s$. "Rigid ground" test case.

	$\Delta t = 2 \cdot 10^{-3}\,s$	$\Delta t = 1 \cdot 10^{-3}\,s$	$\Delta t = 2 \cdot 10^{-4}\,s$
Contact time $[s]$	0.176	0.177	0.1904
Maximum height time $[s]$	0.192	0.193	0.2072

Table 1: Contact time and maximum height time after rebound (related to the minimum distance of the ball from the wall) for the three time steps considered. "Rigid ground" test case.

magnitude and the solution exhibits some oscillations before the contact.

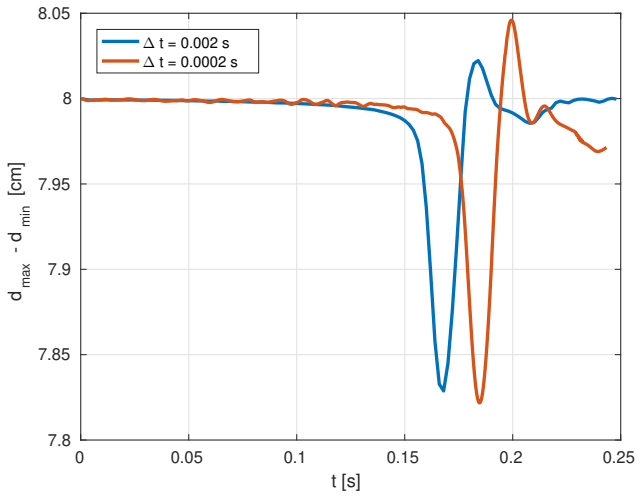

Figure 12: Comparison of the top/bottom distance between the case $\Delta t = 2 \cdot 10^{-3}\, s$ and $\Delta t = 2 \cdot 10^{-4}\, s$. "Rigid ground" test case.

In Figure 13 we plot the fluid vector velocities and vorticity isolines at the instant of contact after rebound for the case $\Delta t = 2 \cdot 10^{-3}\, s$ and for the case $\Delta t = 2 \cdot 10^{-4}\, s$.

4.3 Free fall of an elastic ball on a flexible ground

In this test, we consider a similar configuration to the one used for the test in Section 4.1. In this case, we have a flexible master domain $\widehat{\Omega}^m$ of size $20\, cm \times 0.2\, cm$ with the bottom left corner placed in $(-10, -0.2)\, cm$ and the center of the slave domain $\widehat{\Omega}^s$ is located at the point $(0, 7)\, cm$. We denote with $\Omega = (-10, 10) \times (-0.2, 15)\, cm^2$ the union of the fluid and solids domains, see Figure 14. The initial minimum distance between the master and slave is $1\, cm$.

As in the previous tests, on the ball $\Omega^s(t)$ acts a gravity force $\mathbf{f}^s = (0, -10^3)\, cm/s^2$. The flexible ground $\Omega^m(t)$ is clamped at the bottom and at the lateral boundaries, while the upper side is free to move. No body-force acts on the master body. Due to the symmetry with respect to the vertical axis, in the numerical simulations we consider only half of the domain, see Figure 15. We use the physical parameters described in Section 4.1, where the Lamé coefficients are the same for the slave and master bodies.

For the background mesh, we use a spatial resolution of about $0.5\, cm$ in the upper part and of $0.05\, cm$ in the lower part. For the slave mesh, we use a space discretization of $0.1\, cm$, while for the master body of $0.3\, cm$. We use a time step $\Delta t = 10^{-3}\, s$. Finally, we set the same penalty parameters reported Section 4.1 and $\varepsilon = h$, see Remark 2.

In Figure 16 (left), we show the top/bottom distance of the slave domain. As for the case of contact with a rigid ground, the ball slows down before the activation of the

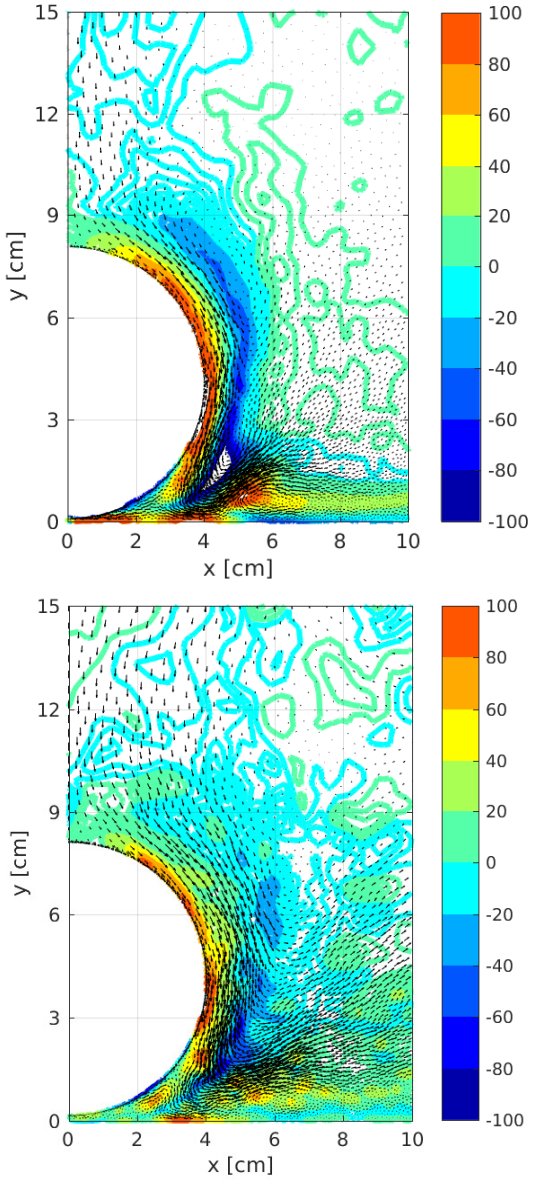

Figure 13: Vorticity and velocity vectors at the instant of contact after rebound. Top: results for $\Delta t = 2 \cdot 10^{-3}\, s$. Bottom: results for $\Delta t = 2 \cdot 10^{-4}\, s$. "Rigid ground" test case.

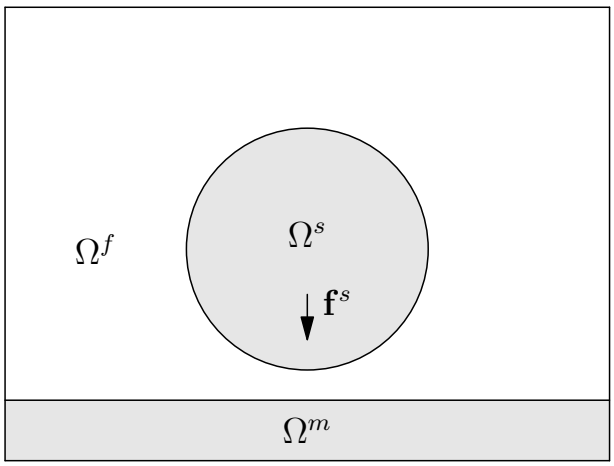

Figure 14: Sketch of the domains $\Omega^f(t)$, $\Omega^s(t)$ and $\Omega^m(t)$. "Flexible ground" test case.

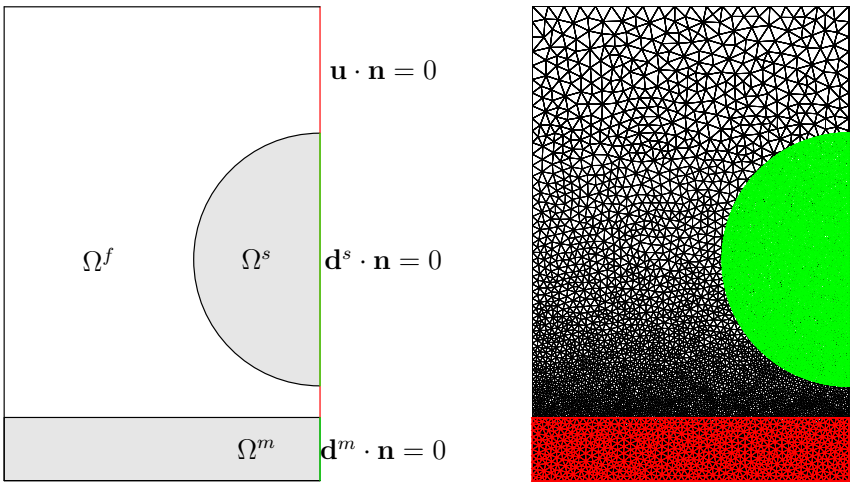

Figure 15: Left: sketch of the reduced domain with the boundary conditions at the symmetry axis (red for the fluid, green for the solids). Right: sketch of the slave body (green) and master one (red). "Flexible ground" test case.

contact due to the high fluid pressure. At time $0.081\ s$ the two bodies come into contact. As for the case of the rigid ground, the ball does not show any further compression at contact but, due to the insufficient internal energy, at time $0.089\ s$, the ball shows a further compression due to the inability to bounce off the flexible wall. From this point on, the two bodies stays in contact.

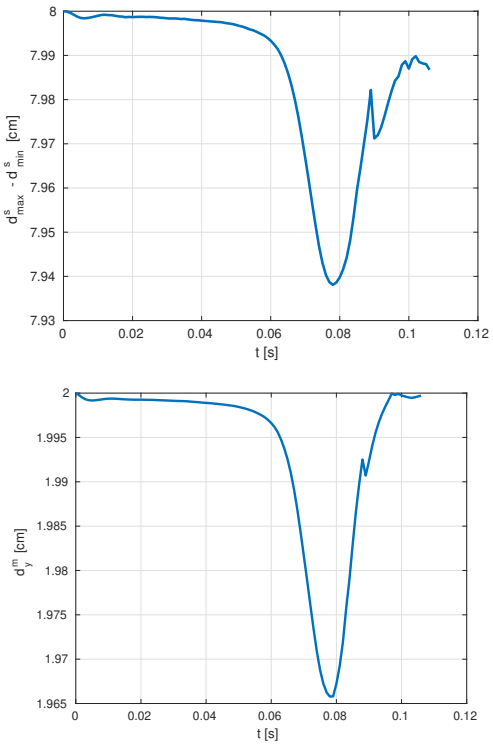

Figure 16: Left: top/bottom distance of the slave body. Right: minimum thickness of the master body. "Flexible ground" test case.

In Figure 17, we plot the displacement isolines at the instant of contact. During contact the minimum distance between the two bodies is about 50% of the local mesh size.

This example shows how the flexibility of the wall dissipates some of the kinetic and internal energy of the ball, stopping it from bouncing away.

5 Conclusions

In this work, we have proposed a penalization contact method in a XFEM/DG numerical framework for the study of FSI problems with contact in the case of large deformations and large displacements. This approach is relatively easy to implement and is very effective. However, it does not guarantee consistency of the numerical method and the formulation requires the penalty term to be sufficiently high in order to ensure

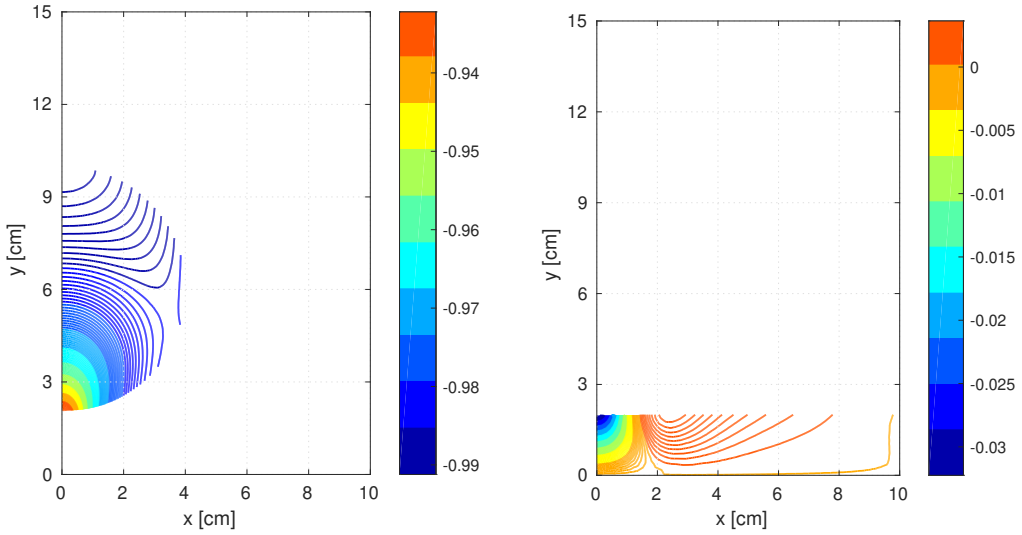

Figure 17: Slave (left) and master (right) vertical displacement isolines at the instant of contact. "Flexible ground" test case.

numerical stability, possibly leading to an ill-conditioned matrix. A possible way to overcame these issues is to consider a Nitsche's approach. Indeed, it produces a consistent formulation and allows to achieve stability with a lower penalty coefficient, see e.g. [18].

We have shown three examples of increasing geometrical complexity: the contact algorithm performs correctly for the "virtual barrier" test case, although the contact with the rigid and flexible ground test cases present some issues in properly reproducing the bouncing of the ball. In fact, the nature of contact requires to have both a sufficiently high spatial and temporal resolutions to catch the correct behaviour. Moreover, the contact model and the coupling conditions with the fluid on the contact region can be improved to obtain a more physical representation of the phenomena, as proposed in [18] and [1].

Even though the numerical tests are performed on 2D geometrical configurations, the proposed algorithm is suited also for simulating more complex scenarios in 3D.

Acknowledgements

The authors gratefully acknowledge the financial support of the Italian MIUR by the grant PRIN12, number 201289A4LX, "Mathematical and numerical models of the cardiovascular system, and their clinical applications". S. Zonca has been supported by "GNCS-INdAM".

References

[1] C. Ager, B. Schott, A.-T. Vuong, A. Popp, and W. A. Wall. A consistent approach for fluid-structure-contact interaction based on a porous flow model for rough surface contact. *International Journal for Numerical Methods in Engineering*, 2018.

[2] C. Ager, A. Seitz, and W. A. Wall. A consistent and comprehensive computational approach for general fluid-structure-contact interaction problems. *arXiv preprint arXiv:1905.09744*, 2019.

[3] P. Alart and A. Curnier. A mixed formulation for frictional contact problems prone to newton like solution methods. *Computer Methods in Applied Mechanics and Engineering*, 92(3):353 – 375, 1991.

[4] F. Alauzet, B. Fabrèges, M. A. Fernández, and M. Landajuela. Nitsche-XFEM for the coupling of an incompressible fluid with immersed thin-walled structures. *Computer Methods in Applied Mechanics and Engineering*, 301:300–335, 2016.

[5] P. Antonietti, M. Verani, C. Vergara, and S. Zonca. Numerical solution of fluid-structure interaction problems by means of a high order Discontinuous Galerkin method on polygonal grids. *Finite Elements in Analysis and Design*, 159:1–14, 2019.

[6] D. Arnold, F. Brezzi, B. Cockburn, and L. Marini. Unified analysis of discontinuous Galerkin methods for elliptic problems. *SIAM Journal on Numerical Analysis*, 39(5):1749–1779, 2002.

[7] F.P.T. Baaijens. A fictitious domain/mortar element method for fluid–structure interaction. *International Journal for Numerical Methods in Fluids*, 35(7):743–761, 2001.

[8] S. Basting, A. Quaini, S. Čanić, and R. Glowinski. Extended ALE Method for fluid–structure interaction problems with large structural displacements. *Journal of Computational Physics*, 331:312–336, 2017.

[9] Y Bazilevs, M-C Hsu, J Kiendl, R Wüchner, and K-U Bletzinger. 3d simulation of wind turbine rotors at full scale. part ii: Fluid–structure interaction modeling with composite blades. *International Journal for numerical methods in fluids*, 65(1-3):236–253, 2011.

[10] Yuri Bazilevs, Victor M Calo, Yongjie Zhang, and Thomas JR Hughes. Isogeometric fluid–structure interaction analysis with applications to arterial blood flow. *Computational Mechanics*, 38(4-5):310–322, 2006.

[11] T. Belytschko, N. Moës, S. Usui, and C. Parimi. Arbitrary discontinuities in finite elements. *International Journal for Numerical Methods in Engineering*, 50(4):993–1013, 2001.

[12] D. Boffi and L. Gastaldi. A fictitious domain approach with Lagrange multiplier for fluid-structure interactions. *Numerische Mathematik*, 135(3):711–732, 2017.

[13] Daniele Boffi and Lucia Gastaldi. A finite element approach for the immersed boundary method. *Computers & structures*, 81(8-11):491–501, 2003.

[14] Daniele Boffi, Lucia Gastaldi, and Luca Heltai. Numerical stability of the finite element immersed boundary method. *Mathematical Models and Methods in Applied Sciences*, 17(10):1479–1505, 2007.

[15] I. Borazjani. Fluid–structure interaction, immersed boundary-finite element method simulations of bio-prosthetic heart valves. *Computer Methods in Applied Mechanics and Engineering*, 257:103–116, 2013.

[16] I. Borazjani, L. Ge, and F. Sotiropoulos. Curvilinear immersed boundary method for simulating fluid structure interaction with complex 3D rigid bodies. *Journal of Computational physics*, 227(16):7587–7620, 2008.

[17] E. Burman, M. Fernández, and P. Hansbo. Continuous interior penalty finite element method for oseen's equations. *SIAM Journal on Numerical Analysis*, 44(3):1248–1274, 2006.

[18] E. Burman, M. A. Fernández, and S. Frei. A Nitsche-based formulation for fluid-structure interactions with contact. *arXiv preprint arXiv:1808.08758*, 2018.

[19] E. Burman, P. Hansbo, and M. G. Larson. Augmented Lagrangian and Galerkin least-squares methods for membrane contact. *International Journal for Numerical Methods in Engineering*, 114(11):1179–1191, 2018.

[20] E. Burman, P. Hansbo, and M. G. Larson. Augmented Lagrangian finite element methods for contact problems. *ESAIM: Mathematical Modelling and Numerical Analysis*, 53(1):173–195, 2019.

[21] Erik Burman. Ghost penalty. *Comptes Rendus Mathematique*, 348(21):1217 – 1220, 2010.

[22] Erik Burman and Miguel A Fernández. Stabilized explicit coupling for fluid–structure interaction using Nitsche's method. *Comptes Rendus Mathematique*, 345(8):467–472, 2007.

[23] Erik Burman and Miguel A. Fernández. An unfitted Nitsche method for incompressible fluid-structure interaction using overlapping meshes. *Computer Methods in Applied Mechanics and Engineering*, 279:497 – 514, 2014.

[24] F. Chouly, M. Fabre, P. Hild, R. Mlika, J. Pousin, and Y. Renard. An overview of recent results on Nitsche's method for contact problems. In S. P. A. Bordas, E. Burman, M. G. Larson, and M. A. Olshanskii, editors, *Geometrically unfitted finite element methods and applications*, pages 93–141. Springer International Publishing, 2017.

[25] F. Chouly and P. Hild. A Nitsche-based method for unilateral contact problems: Numerical analysis. *SIAM Journal on Numerical Analysis*, 51(2):1295–1307, 2013.

[26] F. Chouly and P. Hild. On convergence of the penalty method for unilateral contact problems. *Applied Numerical Mathematics*, 65:27–40, 2013.

[27] F. Chouly, R. Mlika, and Y. Renard. An unbiased Nitsche's approximation of the frictional contact between two elastic structures. *Numerische Mathematik*, 139(3):593–631, 2018.

[28] F. Chouly and Y. Renard. Explicit Verlet time-integration for a Nitsche-based approximation of elastodynamic contact problems. *Advanced Modeling and Simulation in Engineering Sciences*, 5(1):31, 2018.

[29] J. Donea, S. Giuliani, and J.P. Halleux. An arbitrary Lagrangian-Eulerian finite element method for transient dynamic fluid-structure interactions. *Computer Methods in Applied Mechanics and Engineering*, 33(1):689–723, 1982.

[30] C. Farhat, M. Lesoinne, and P. Le Tallec. Load and motion transfer algorithms for fluid/structure interaction problems with non-matching discrete interfaces: Momentum and energy conservation, optimal discretization and application to aeroelasticity. *Computer Methods in Applied Mechanics and Engineering*, 157(1-2):95–114, 1998.

[31] L. Formaggia and F. Nobile. A stability analysis for the arbitrary Lagrangian Eulerian formulation with finite elements. *East-West Journal of Numerical Mathematics*, 7(2):105–132, 1999.

[32] L. Formaggia, C. Vergara, and S. Zonca. Unfitted extended finite elements for composite grids. *Computers & Mathematics with Applications*, 76(4):893–904, 2018.

[33] S. Frei. *Eulerian finite element methods for interface problems and fluid-structure interactions*. PhD thesis, Heidelberg University, 2016.

[34] S. Frei, T. Richter, and T. Wick. Long-term simulation of large deformation, mechano-chemical fluid-structure interactions in ALE and fully Eulerian coordinates. *Journal of Computational Physics*, 321(Supplement C):874–891, 2016.

[35] A. Gerstenberger and W. A. Wall. An extended finite element method/Lagrange multiplier based approach for fluid–structure interaction. *Computer Methods in Applied Mechanics and Engineering*, 197(19):1699–1714, 2008.

[36] R. Glowinski, T.-W. Pan, and J. Periaux. A fictitious domain method for Dirichlet problem and applications. *Computer Methods in Applied Mechanics and Engineering*, 111(3-4):283–303, 1994.

[37] B. E. Griffith. Immersed boundary model of aortic heart valve dynamics with physiological driving and loading conditions. *International Journal for Numerical Methods in Biomedical Engineering*, 28(3):317–345, 2012.

[38] Anita Hansbo and Peter Hansbo. A finite element method for the simulation of strong and weak discontinuities in solid mechanics. *Computer Methods in Applied Mechanics and Engineering*, 193(33):3523 – 3540, 2004.

[39] C. W. Hirt, A. A. Amsden, and J. L. Cook. An arbitrary Lagrangian-Eulerian computing method for all flow speeds. *Journal of Computational Physics*, 14(3):227–253, 1974.

[40] Noboru Kikuchi and John Tinsley Oden. *Contact problems in elasticity: a study of variational inequalities and finite element methods*, volume 8. siam, 1988.

[41] LifeV. http://www.lifev.org.

[42] Y. Liu and W. K. Liu. Rheology of red blood cell aggregation by computer simulation. *Journal of Computational Physics*, 220(1):139–154, 2006.

[43] Gil Marom. Numerical methods for fluid–structure interaction models of aortic valves. *Archives of Computational Methods in Engineering*, 22(4):595–620, 2015.

[44] A. Massing, M. G. Larson, A. Logg, and M. E. Rognes. A Nitsche-based cut finite element method for a fluid-structure interaction problem. *Communications in Applied Mathematics and Computational Science*, 10(2):97–120, 2015.

[45] R. Mittal and G. Iaccarino. Immersed boundary methods. *Annual Review of Fluid Mechanics*, 37(1):239–261, 2005.

[46] N. Moës, J. Dolbow, and T. Belytschko. A finite element method for crack growth without remeshing. *International Journal for Numerical Methods in Engineering*, 46:131–150, September 1999.

[47] E. Oñate, M. A. Celigueta, S. R. Idelsohn, F. Salazar, and B. Suárez. Possibilities of the particle finite element method for fluid–soil–structure interaction problems. *Computational Mechanics*, 48(3):307–318, 2011.

[48] N.A. Patankar, P. Singh, D.D. Joseph, R. Glowinski, and T.-W. Pan. A new formulation of the distributed Lagrange multiplier/fictitious domain method for particulate flows. *International Journal of Multiphase Flow*, 26(9):1509–1524, 2000.

[49] C. S. Peskin. Flow patterns around heart valves: a numerical method. *Journal of computational physics*, 10(2):252–271, 1972.

[50] C. S. Peskin. The immersed boundary method. *Acta Numerica*, 11:479–517, 1 2002.

[51] R. Rannacher and T. Richter. An adaptive finite element method for fluid-structure interaction problems based on a fully Eulerian formulation. In H.-J. Bungartz, M. Mehl, and M. Schäfer, editors, *Fluid Structure Interaction II: Modelling, Simulation, Optimization*, pages 159–191. Springer Berlin Heidelberg, Berlin, Heidelberg, 2010.

[52] G. Rega. Nonlinear vibrations of suspended cables–Part I: Modeling and analysis. *Applied Mechanics Reviews*, 57(6):443–478, 2004.

[53] T. Richter. A fully Eulerian formulation for fluid–structure-interaction problems. *Journal of Computational Physics*, 233:227–240, 2013.

[54] T. Richter and T. Wick. Finite elements for fluid–structure interaction in ALE and fully Eulerian coordinates. *Computer Methods in Applied Mechanics and Engineering*, 199(41):2633–2642, 2010.

[55] P. H. Saksono, W. G. Dettmer, and D. Perič. An adaptive remeshing strategy for flows with moving boundaries and fluid-structure interaction. *International Journal for Numerical Methods in Engineering*, 71(9):1009–1050, 2007.

[56] C. Vergara and S. Zonca. Extended finite elements method for fluid-structure interaction with an immersed thick non-linear structure. In D. Boffi, L. Pavarino, G. Rozza, S. Scacchi, and C. Vergara, editors, *Mathematical and Numerical Modeling of the Cardiovascular System and Applications - SEMA SIMAI Springer Series*, pages 209–243. Springer, 2018.

[57] Peter Wriggers and Giorgio Zavarise. Computational contact mechanics. *Encyclopedia of computational mechanics*, 2004.

[58] D. Xu, E. Kaliviotis, A. Munjiza, E. Avital, C. Ji, and J. Williams. Large scale simulation of red blood cell aggregation in shear flows. *Journal of Biomechanics*, 46(11):1810–1817, 2013.

[59] H. Zhang, L. Liu, M. Dong, and H. Sun. Analysis of wind-induced vibration of fluid–structure interaction system for isolated aqueduct bridge. *Engineering structures*, 46:28–37, 2013.

[60] S. Zonca. *Unfitted numerical methods for fluid-structure interaction arising between an incompressible fluid and an immersed thick structure*. PhD thesis, Politecnico di Milano, 2018.

[61] S. Zonca, C. Vergara, and L. Formaggia. An unfitted formulation for the interaction of an incompressible fluid with a thick structure via an XFEM/DG approach. *SIAM Journal on Scientific Computing*, 40(1):B59–B84, 2018.

MOX Technical Reports, last issues

Dipartimento di Matematica
Politecnico di Milano, Via Bonardi 9 - 20133 Milano (Italy)

42/2019 Martino, A.; Guatteri, G.; Paganoni, A.M.
hmmhdd Package: Hidden Markov Model for High Dimensional Data

43/2019 Antonietti, P.F.; Mazzieri, I.; Migliorini, F.
A space-time discontinuous Galerkin method for the elastic wave equation

41/2019 Abbà, A.; Bonaventura, L.; Recanati, A.; Tugnoli, M.;
Dynamical p-adaptivity for LES of compressible flows in a high order DG framework

38/2019 Massi, M.C.; Ieva, F.; Gasperoni, F.; Paganoni, A.M.
Minority Class Feature Selection through Semi-Supervised Deep Sparse Autoencoders

39/2019 Lovato, I.; Pini, A.; Stamm, A.; Taquet, M.; Vantini, S.
Multiscale null hypothesis testing for network-valued data: analysis of brain networks of patients with autism

40/2019 Lovato, I.; Pini, A.; Stamm, A.; Vantini, S.
Model-free two-sample test for network-valued data

36/2019 Salvador, M.; Dede', L.; Quarteroni, A.
An intergrid transfer operator using radial basis functions with application to cardiac electromechanics

37/2019 Menafoglio, A.; Secchi, P.
O2S2: a new venue for computational geostatistics

34/2019 Antonietti, P. F.; Mazzieri, I.; Melas, L.; Paolucci, R.; Quarteroni, A.; Smerzini, C.; Stupazzini,
Three-dimensional physics-based earthquake ground motion simulations for seismic risk assessment in densely populated urban areas

35/2019 Zancanaro, M.; Ballarin, F.; Perotto, S.; Rozza, G.
Hierarchical model reduction techniques for flow modeling in a parametrized setting